International Journal of Solids and Structures 71 (2015) 277–290

Contents lists available at ScienceDirect

International Journal of Solids and Structures

journal homepage: www.elsevier.com/locate/ijsolstr

A mesoscopic theory of dislocation and disclination fields for grain boundary-mediated crystal plasticity

V. Taupin [a,*], L. Capolungo [b], C. Fressengeas [a], M. Upadhyay [b], B. Beausir [a]

[a] Laboratoire d'Etude des Microstructures et de Mécanique des Matériaux, Université de Lorraine/CNRS, Ile du Saulcy, 57045 Metz Cedex, France
[b] G.W. Woodruff School of Mechanical Engineering, Georgia Institute of Technology/CNRS, 57070 Metz Cedex, France

ARTICLE INFO

Article history:
Received 20 December 2014
Received in revised form 5 May 2015
Available online 6 July 2015

Keywords:
Grain boundary
Disclination
Dislocation

ABSTRACT

A coarse-grained extension of a recent nanoscale elasto-plastic model of polar dislocation and disclination density fields is developed to model grain boundary-mediated plasticity in polycrystals. At a small resolution length scale, the polar dislocation/disclination densities render continuously the discontinuities of the elastic displacements/rotations across grain boundaries. When the resolution length scale increases, the net polarities of a crystal defect ensemble decrease, perhaps to the point where no strain/curvature incompatibility is left in the body. The defect densities are then labeled "statistical". However both polar and statistical dislocation/disclination densities contribute to plastic flow, and a coarse-grained mesoscopic plastic curvature rate needs to be defined. In addition, whereas it is overlooked at nanoscale where grain boundaries are seen as continua, tangential continuity of the elastic/plastic curvature/strain rates across grain boundaries needs to be considered at mesoscale, because the latter are seen as singular discontinuity interfaces. It induces long-range, grain-to-grain, elastic/plastic interactions across interfaces. The mesoscale model allow preserving the essential features of the lower scale approach. In particular, it is shown that it allows accounting for such plastic deformation mechanisms as grain boundary migration and grain boundary misorientation variation by disclination motion and concurrent dislocation nucleation, when plasticity by dislocation glide is unavailable. Accumulation of polar defect densities in the vicinity of the grain boundaries and triple lines, leading to long-range inter-granular activation of slip and grain size effects, are also predicted by the model.

1. Introduction

In polycrystals, grain boundaries (GBs) are thin regions where the lattice rapidly changes its orientation within nanometers (Sutton and Vitek, 1983; Priester, 2013; Fressengeas et al., 2014; Cordier et al., 2014). GBs play a key role in the mechanical response of polycrystals. They can strengthen the materials by limiting dislocation glide within grains. Dislocation transmission or re-emission from GBs do also lead to plastic flow, such that the role of GBs in plasticity is not limited to being obstacles for dislocation glide. In nanocrystalline materials or in slip-deprived materials, GBs can also become important sources of plastic deformation. Well-known examples of GB-mediated plasticity mechanisms are GB migration (Gutkin and Ovid'ko, 2005; Farkas et al., 2006; Cahn et al., 2006; Ovid'ko et al., 2008; Gorkaya et al., 2009; Mompiou et al., 2009; Cordier et al., 2014), nucleation of dislocations (Tschopp et al., 2007, 2008) followed by propagation in grains (Van Swygenhoven et al., 2006, 2008; Bitzek et al., 2008). Importantly, the elasto-plastic response of nanocrystalline materials is strongly sensitive to the atomic structure of the GBs (McDowell, 2008). For example, the atomic structural units and associated excess free volumes (Tucker et al., 2010a) composing the GBs (Sutton and Vitek, 1983) were shown to correlate with both nucleation of dislocations at GBs (Tucker et al., 2010a) and shear-coupled boundary migration (Cahn et al., 2006; Taupin et al., 2014).

Several modeling approaches aimed at describing the mechanical response of GBs and phase boundaries in relation with the interface microstructure have been developed in the past (see e.g. Bollmann, 1970; Pond and Hirth, 1994; Hirth and Pond, 1996; Hirth et al., 2006; Khater et al., 2012; Vattre et al., 2014). In particular, elasto-static disclination-based approaches have been proposed (Romanov and Kolesnikova, 2009; Romanov et al., 2015; Li, 1972; Shih and Li, 1975; Gertsman et al., 1989), which successfully complemented dislocation-based models and motivated further investigation involving dissipative processes. Indeed, in past work by the authors, a nanoscale structure sensitive

* Corresponding author.
E-mail address: vincent.taupin@univ-lorraine.fr (V. Taupin).

http://dx.doi.org/10.1016/j.ijsolstr.2015.06.031
0020-7683/

model of GBs was proposed within the framework of an elasto-plastic theory of disclination and dislocation fields (Fressengeas et al., 2011). In this theory, based on seminal works by Volterra (1907), Nye (1953), Mura (1963), deWit (1970), Kröner (1980) and Acharya (2001), the polar disclination and dislocation densities account in a continuous manner for the discontinuities of the elastic/plastic rotation and displacement arising across bounded surfaces in a crystalline material. These defect densities induce incompatible elastic and plastic curvatures and strains, leading to long-range internal stress and couple stress fields. Their transport, driven by thermodynamically consistent mechanical forces, provides their spatio-temporal dynamics and yields plastic deformation (Fressengeas et al., 2011). This theory was first used for continuous modeling of the core structure of symmetric tilt boundaries in copper (Fressengeas et al., 2014) and more complex boundaries in olivine (Cordier et al., 2014) and fullerene monolayers (Bozhko et al., 2014). In these papers, an atomistic to continuum crossover is realized by substituting dipoles of wedge disclination densities to the structural units composing the core of the GBs (Sutton and Vitek, 1983). A continuous distribution of elastic energy in the GB core area is obtained from the solution of the field equations, in good agreement with atomistic simulations and experiments (Hasson et al., 1972; Tschopp et al., 2008). Based on this structure of disclination dipoles, shear-coupled boundary migration of symmetric tilt boundaries in copper is also retrieved (Taupin et al., 2014), in agreement with atomistic and experimental findings (Cahn et al., 2006; Gorkaya et al., 2009). An essential outcome of the model is that, since the discrete atomic structures are replaced by continuous defect densities, the vibrations of atoms do not have to be resolved at the femto-second time scale. Thus, time-coarsening is built-in, which allows performing simulations over realistic time scales with strain rate levels amounting to experimental values (Taupin et al., 2014), while keeping essential features of GBs.

The objective of the present study is to provide a coarse-grained extension of the above Field Dislocation and Disclination Mechanics (FDDM) nanoscale framework that allows retaining some of its key features at mesoscale, namely, the ability to account for the structure of GBs in predicting the mechanical response of polycrystalline media. Such an extension requires addressing three fundamental challenges, all arising from the scale dependence of the continuous measures of lattice incompatibility in the presence of crystal defects. First, although the array of disclination dipoles composing the GB structure at nanoscale is overlooked when the resolution length scale is increased in the coarse-graining process, recent measurements obtained from EBSD orientation maps reveal the presence of dislocation and disclination dipoles decorating GBs and triple lines at mesoscale (Beausir and Fressengeas, 2013). Hence, a first challenge will be to account for such mesoscale patterns of crystal defects and their spatio-temporal evolution. Second, whereas GBs are seen as continua in the nanoscale FDDM framework, the mesoscale approach promoted here will adopt an interfacial description of the GBs – *i.e.* GBs of vanishingly small thickness. Hence, the second point to be addressed in the present paper is the account of continuity conditions at interfaces on the strain/curvature tensors, traction vector and elastic/plastic strain/curvature tensors (Acharya, 2007; Fressengeas et al., 2012), which allow retaining the nonlocal features of the GBs that are essential to render the grain-to-grain interactions and their consequences on plastic strain and orientation distributions (textures), and mechanical behavior. Third, whereas the coarse-graining process leads to decreasing crystal defect densities when the resolution length scale is increased, it does not impact on the plastic distortion and curvature rates, which do not follow this decreasing trend (Fressengeas et al., 2012). As a result, mesoscale plastic distortion and curvature rates statistically offsetting for the decreasing polar plastic distortion and curvature rates need to be introduced in the averaging process, in analogy with the work by Acharya and Roy (2006) in the pure dislocation case. A finite element implementation of the proposed phenomenological mesoscopic field disclination and dislocation mechanics (PMFDDM) model will be developed, in order to show illustrative examples and to evidence the predictive potential brought by the model in mesoscale systems.

The paper is organized as follows. In Section 2, useful mathematical notations are settled. In Section 3, the mesoscale extension of the model is introduced. Essential points in this section are the scale dependence of polar defect densities, the initial representation of GBs at mesoscale, and the implementation of tangential continuity conditions on plastic distortion and curvature rates at singular GB interfaces. The coarse-grain derivation of a mesoscale statistical plastic curvature rate, an analysis of scale dependences of the PMFDDM model as well as the ability of the latter to render new GB-driven plastic mechanisms, are discussed in Section 4. In Section 5, illustrative simulations of bicrystals and tricrystals are presented to show the predictive capability of the model. Conclusions follow.

2. Notations

A bold symbol denotes a tensor. When there may be ambiguity, an arrow is superposed to represent a vector: $\vec{\mathbf{V}}$. The symmetric part of tensor $\mathbf{A}$ is denoted $\mathbf{A}^{sym}$. Its skew-symmetric part is $\mathbf{A}^{skew}$. The tensor $\mathbf{A}\cdot\mathbf{B}$, with rectangular Cartesian components $A_{ik}B_{kj}$, results from the dot product of tensors $\mathbf{A}$ and $\mathbf{B}$, and $\mathbf{A}\otimes\mathbf{B}$ is their tensorial product, with components $A_{ij}B_{kl}$. A: represents the trace inner product of the two second order tensors $\mathbf{A}:\mathbf{B}=A_{ij}B_{ij}$, in rectangular Cartesian components, or the product of a higher order tensor with a second order tensor, e.g., $\mathbf{A}:\mathbf{B}=A_{ijkl}B_{kl}$. The cross product of a second-order tensor $\mathbf{A}$ and a vector $\mathbf{V}$, the **div** and **curl** operations for second-order tensors are defined row by row, in analogy with the vectorial case. For any base vector $\mathbf{e}_i$ of the reference frame:

$$(\mathbf{A}\times\mathbf{V})^t\cdot\mathbf{e}_i=(\mathbf{A}^t\cdot\mathbf{e}_i)\times\mathbf{V}, \tag{1}$$

$$(\mathbf{div}\mathbf{A})^t\cdot\mathbf{e}_i=\mathbf{div}(\mathbf{A}^t\cdot\mathbf{e}_i), \tag{2}$$

$$(\mathbf{curl}\mathbf{A})^t\cdot\mathbf{e}_i=\mathbf{curl}(\mathbf{A}^t\cdot\mathbf{e}_i). \tag{3}$$

In rectangular Cartesian components:

$$(\mathbf{A}\times\mathbf{V})_{ij}=e_{jkl}A_{ik}V_l, \tag{4}$$

$$(\mathbf{div}\mathbf{A})_i=A_{ij,j}, \tag{5}$$

$$(\mathbf{curl}\mathbf{A})_{ij}=e_{jkl}A_{il,k}. \tag{6}$$

where e_{jkl} is a component of the third-order alternating Levi–Civita tensor $\mathbf{X}$. A vector $\vec{\mathbf{A}}$ is associated with tensor $\mathbf{A}$ by using its trace inner product with tensor $\mathbf{X}$:

$$(\vec{\mathbf{A}})_k=-\frac{1}{2}(\mathbf{A}:\mathbf{X})_k=-\frac{1}{2}e_{ijk}A_{ij}. \tag{7}$$

In the component representation, the spatial derivative with respect to a Cartesian coordinate is indicated by a comma followed by the component index. A superposed dot represents a material time derivative. Finally, $[\mathbf{A}]=\mathbf{A}^+-\mathbf{A}^-$ denotes a jump or a discontinuity of tensor $\mathbf{A}$ across an oriented interface.

3. Mesoscale model of dislocation and disclination fields

3.1. Polar defect densities

The field theory of dislocations and disclinations is now briefly recalled, the reader is referred to the paper by Fressengeas et al. (2011) for a more comprehensive presentation. In a continuum mechanics setting in the absence of cracks, the displacement vector field $\mathbf{u}$ is defined continuously at any point of an elasto-plastic body. The total distortion tensor, defined as the gradient of the displacement $\mathbf{U} = \mathbf{gradu}$, is thus curl-free:

$$\mathbf{curl}\,\mathbf{U} = 0. \tag{8}$$

In the presence of dislocation ensembles (Acharya, 2001), the plastic, $\mathbf{U_p}$, and elastic, $\mathbf{U_e}$, components of the distortion may contain incompatible, non curl-free parts, $\mathbf{U_p^{\perp}}$ and $\mathbf{U_e^{\perp}}$. Additional curl-free compatible components, $\mathbf{U_e^{\parallel}}$ and $\mathbf{U_p^{\parallel}}$, allow satisfying the balance of equilibrium and boundary conditions. The following relations are therefore satisfied:

$$\mathbf{U} = \mathbf{U_e} + \mathbf{U_p}, \tag{9}$$

$$\mathbf{U_e} = \mathbf{U_e^{\perp}} + \mathbf{U_e^{\parallel}}, \tag{10}$$

$$\mathbf{U_p} = \mathbf{U_p^{\perp}} + \mathbf{U_p^{\parallel}}, \tag{11}$$

$$0 = \mathbf{U_e^{\perp}} + \mathbf{U_p^{\perp}}, \tag{12}$$

$$\mathbf{curl}\,\mathbf{U_e^{\perp}} = -\mathbf{curl}\,\mathbf{U_p^{\perp}} = \boldsymbol{\alpha} \neq 0. \tag{13}$$

Eq. (13) are satisfied by the incompatible plastic distortion $\mathbf{U_p^{\perp}}$ associated with the presence of Nye's polar dislocation density tensor $\boldsymbol{\alpha}$ (Nye, 1953), and by the incompatible elastic distortion $\mathbf{U_e^{\perp}}$ ensuring the continuity of matter implied by Eq. (8). The polar dislocation density can be used to represent the core of a single or partial dislocation as well as an ensemble of dislocations with non-zero net Burgers vector. Since $\mathbf{U_e^{\parallel}}$ and $\mathbf{U_p^{\parallel}}$ are curl-free, Eq. (13) can also be written as:

$$\mathbf{curl}\,\mathbf{U_e} = -\mathbf{curl}\,\mathbf{U_p} = \boldsymbol{\alpha}. \tag{14}$$

By decomposing the elastic and plastic distortions into their symmetric and skew-symmetric parts, Eq. (14) can alternatively be expressed as (deWit, 1970; Fressengeas et al., 2011):

$$\mathbf{curl}\,\boldsymbol{\epsilon}_e = +\boldsymbol{\alpha} + \boldsymbol{\kappa}_e^t - tr(\boldsymbol{\kappa}_e)\mathbf{I}, \tag{15}$$

$$\mathbf{curl}\,\boldsymbol{\epsilon}_p = -\boldsymbol{\alpha} + \boldsymbol{\kappa}_p^t - tr(\boldsymbol{\kappa}_p)\mathbf{I}. \tag{16}$$

Eqs. (15) and (16) relate the incompatibilities in elastic strain $\boldsymbol{\epsilon}_e$ and plastic strain $\boldsymbol{\epsilon}_p$ arising from the presence of Nye's dislocation density tensor $\boldsymbol{\alpha}$, and the elastic, $\boldsymbol{\kappa}_e$, and plastic curvature, $\boldsymbol{\kappa}_p$. In an elasto-plastic model considering solely dislocations, the elastic, plastic and total, $\boldsymbol{\kappa}$, curvature tensors are rotation gradients:

$$\boldsymbol{\kappa}_e = \mathbf{grad}\,\vec{\boldsymbol{\omega}}_e, \tag{17}$$

$$\boldsymbol{\kappa}_p = \mathbf{grad}\,\vec{\boldsymbol{\omega}}_p, \tag{18}$$

$$\mathbf{grad}\,\vec{\boldsymbol{\omega}} = \boldsymbol{\kappa} = \boldsymbol{\kappa}_e + \boldsymbol{\kappa}_p. \tag{19}$$

Hence, the elastic and plastic curvatures are curl-free and the associated rotation vectors $(\vec{\boldsymbol{\omega}}_e, \vec{\boldsymbol{\omega}}_p)$ are integrable single-valued quantities. The sum of the elastic and plastic rotation vectors is the material rotation vector $\vec{\boldsymbol{\omega}} = \frac{1}{2}\mathbf{curl}\,\mathbf{u}$. As shown by deWit (1970), $(\boldsymbol{\kappa}_e, \boldsymbol{\kappa}_p)$ may not be curl-free anymore, if the possibility of multi-valued elastic and plastic rotations $\vec{\boldsymbol{\omega}}_e$ and $\vec{\boldsymbol{\omega}}_p$, *i.e.*, a discontinuity of the elastic and plastic rotations over some surface, is acknowledged. In such a situation, a non-zero tensor $\boldsymbol{\theta}$ such that

$$\boldsymbol{\theta} = -\mathbf{curl}\,\boldsymbol{\kappa}_p = \mathbf{curl}\,\boldsymbol{\kappa}_e \tag{20}$$

can be defined. $\boldsymbol{\theta}$ is the polar disclination density tensor (deWit, 1970). Similarly to the case of dislocations, the incompatible part of the plastic curvature tensor due to a polar disclination density is offset by the incompatible part of the elastic curvature tensor in order to ensure the continuity of matter. Since the rotation vectors $(\vec{\boldsymbol{\omega}}_e, \vec{\boldsymbol{\omega}}_p)$ are multi-valued in the presence of disclinations, the corresponding elastic and plastic rotation and distortion tensors are undefined. The discontinuity of the elastic rotation is the Frank vector. It is obtained by integrating the incompatible elastic curvatures along a closed circuit C:

$$\boldsymbol{\Omega} = \int_C \boldsymbol{\kappa}_e \cdot \mathbf{dr}. \tag{21}$$

Similarly, the discontinuity of the elastic displacement is the Burgers vector. It contains a possible contribution from the non-uniformity of elastic curvatures and reads (deWit, 1970):

$$\mathbf{b} = \int_C (\boldsymbol{\epsilon}_e - (\boldsymbol{\kappa}_e^t \times \mathbf{r})^t) \cdot \mathbf{dr}. \tag{22}$$

If S is the surface of unit normal $\mathbf{n}$ bounded by circuit C, using Stokes's theorem and Eqs. (15) and (20) allows rewriting Eqs. (21) and (22) as:

$$\boldsymbol{\Omega} = \int_S \boldsymbol{\theta} \cdot \mathbf{n} dS, \tag{23}$$

$$\mathbf{b} = \int_S (\boldsymbol{\alpha} - (\boldsymbol{\theta}^t \times \mathbf{r})^t) \cdot \mathbf{n} dS. \tag{24}$$

$\boldsymbol{\Omega}$ and $\mathbf{b}$ defined above are point-wise measures of the lattice incompatibility in the presence of disclinations and dislocations. In contrast, the disclination and dislocation densities $\boldsymbol{\theta}$ and $\boldsymbol{\alpha}$ defined in Eqs. (15) and (20) are continuous tensorial renditions of this incompatibility. They provide a natural regularization of the singular and discontinuous nature of the Frank/Burgers vectors and they are thus appropriate mathematical tools to model the core of crystal defects in a fully continuous fashion.

3.2. Scale dependence of polar defect densities

Eqs. (21)–(24) reveal the circuit size/resolution length scale dependence of the Burgers and Frank vectors and of the corresponding polar defect densities. Given a prescribed ensemble of crystal defects, the Burgers/Frank vectors directly depend on the choice of surface S and on the characteristic size of circuit C. If this size is chosen in the *nm* scale or less, every defect (or part of a defect) can be resolved by a polar defect density, and a complete description of the incompatible elastic strains and curvatures associated with this defect configuration is obtained. For example, considering as in Fig. 1 a dipole of dislocations/disclinations of opposite magnitudes, and adopting a small circuit C allows capturing the Burgers/Frank vector of each individual defect and describing the dipoles with defect densities of opposite signs. Hence, the incompatibility induced by the dipoles is fully captured by the polar defect density field. In contrast, if a mesoscale resolution is chosen, such that the circuit encompasses all defects, then the net polarity of the defect ensemble may reduce or even cancel out. For instance, if one increases circuit C in Fig. 1 to the point where it fully encompasses the dipole, the net Burgers/Frank vectors vanish, as well as the corresponding polar dislocation/disclocation densities. In this extreme case, the incompatibility induced by the dipoles is missed by the representation.

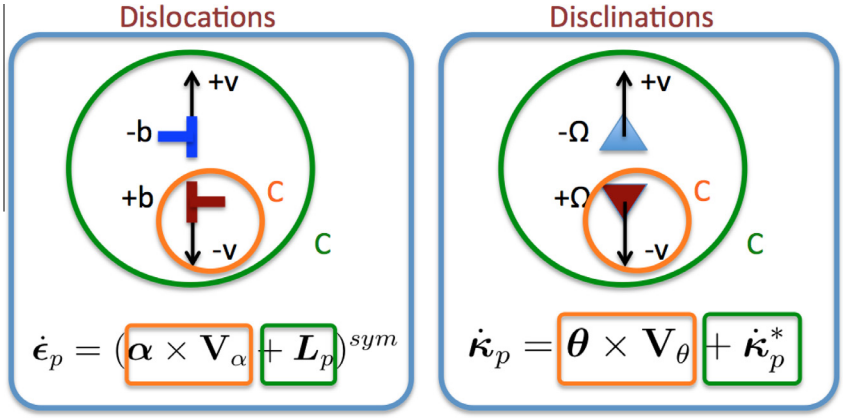

Fig. 1. Scale dependence of polar defect densities and plastic flow. Example of the expansion of an edge dislocation dipole (left) and a wedge disclination dipole (right). At a small nanoscale resolution sketched by the orange Burgers and Frank circuits, each dislocation/disclination can be rendered by a polar dislocation/disclination density. In that case, the plastic strain/curvature rate produced by the expansion of a dislocation/disclination dipole with velocity v can be rendered by the mobility of polar dislocation/disclination densities (terms surrounded by orange lines). At a higher mesoscale resolution sketched by the green circuits, the polarities of the dislocation/disclination dipole "statistically" offset, resulting in a statistical dislocation/disclination density. In that case, the plastic strain/curvature rate produced by the expansion of the dislocation/disclination dipole cannot be resolved by the mobility of polar dislocation/disclination densities and must be accounted for by a statistical rate term (terms surrounded by green lines). (For interpretation of the references to colour in this figure caption, the reader is referred to the web version of this article.)

3.3. Scale dependent representation of grain boundaries

When modeling symmetric tilt GBs with nanoscale resolution, dipoles of polar disclination densities are used to continuously represent the atomic structural units composing GBs (Fressengeas et al., 2014). As per discussion in the above, this construct does not apply at mesoscale resolution, as the net polar disclination density may vanish. From this standpoint, the need for using polar disclination densities may appear as limited at mesoscale. However, even at such a scale, recent estimates from electron back-scattered diffraction (EBSD) orientation maps with sub-micron resolution evidenced the presence of polar disclination dipoles along GBs (Beausir and Fressengeas, 2013). Clearly, these density fields do not render the individual crystal defects constituting the grain boundary structure at nanoscale, but rather the net polarity of ensembles of defects resulting from misorientation gradients at mesoscale along the GBs.

Motivated by these observations, we propose to follow the methodology already used in EBSD orientation mapping to build the fields of incompatibility that will render initial grain boundaries at mesoscale. Interestingly, this allows employing experimental orientation maps to build initial conditions for the crystal defect density fields. Using the Bunge convention, the local lattice orientation is characterized by the set of Euler angles (ϕ_1, ϕ, ϕ_2) and the associated sample-to-crystal rotation matrix $\mathbf{R}$. The disorientation between two points (in EBSD, two pixels) a and b in the body is given by the couple $(\mathbf{r}, \Delta\psi)$, where $\mathbf{r}$ is the axis of rotation and $\Delta\psi$ the disorientation angle around $\mathbf{r}$. In the Cartesian coordinate system with the sample reference frame $(\mathbf{e_1}, \mathbf{e_2}, \mathbf{e_3})$, the difference of elastic rigid body rotation vector $\Delta\boldsymbol{\omega}^e$ between points a and b satisfies:

$$\Delta\psi\mathbf{r} = \Delta\omega_i^e e_i. \tag{25}$$

If $\mathbf{R_a}$ and $\mathbf{R_b}$ denote the rotation matrices at points a and b, the disorientation matrix from point a to b can be calculated as $\Delta\mathbf{R} = \mathbf{R_a}^{-1}.\mathbf{R_b}$. Then, the variation of the elastic rotation $\Delta\omega_i^e$ is obtained from (Pantleon, 2008):

$$\Delta\omega_i^e = -\frac{e_{ijk}\Delta R_{jk}\Delta\psi}{2sin(\Delta\psi)}. \tag{26}$$

As a final step, the elastic curvature tensor component κ_{ij}^e is approximated by the variation of the elastic rigid body rotation $\Delta\omega_i^e$ over a distance Δx_j:

$$\kappa_{ij}^e = \frac{\Delta\omega_i^e}{\Delta x_j}. \tag{27}$$

The initial polar disclination density associated with this elastic curvature field is then given by Eq. (20) $\boldsymbol{\theta} = \mathbf{curl}\,\boldsymbol{\kappa}^e$. Overlooking the curl of elastic strain tensor at the initial time and using Eq. (15), the initial polar dislocation density associated with elastic curvatures is approximately given by:

$$\boldsymbol{\alpha} = -\boldsymbol{\kappa}_e^t + tr(\boldsymbol{\kappa}_e)\mathbf{I}. \tag{28}$$

Because the incompatible elastic strain in Eq. (15) is unknown from orientation mapping, a fraction of the dislocation density is clearly overlooked. Fig. 2 depicts the geometry of micron-sized bicrystal and tricrystal configurations, together with their initial dislocation and disclination density fields. Fig. 2(a) shows the initial edge dislocation density field associated with a tilt boundary in a bicrystal, as obtained from Eqs. (26)–(28). Because periodic boundary conditions are used along the directions of the GB plane, the polar disclination density field is uniformly zero. Fig. 2(b) and (c) show the initial field for the norm of the polar dislocation and disclination density tensors in a tricrystal with three GBs that have each both tilt and twist components, as obtained from Eqs. (20), (26), (27) and (28). Walls of edge and screw polar dislocations are found in the GBs, whereas wedge and twist polar disclinations are observed at the triple line. Disclinations are also present at the intersection of the GBs and external surfaces, in order to terminate GB dislocation walls. The polar defect densities obtained in these simple bicrystal and tricrystal configurations are in good agreement with those observed in EBSD orientation maps (Beausir and Fressengeas, 2013).

To verify consistency of the predictions, the polar dislocation density obtained for the tilt boundary shown in Fig. 2(a) is now explained. The edge polar dislocation density α_{13} obtained follows from Eqs. (27) and (28). The jump of lattice orientation $\Delta\omega_3^e$ across the GB of normal $\mathbf{e_1}$ results in a bending elastic curvature $\kappa_{31}^e = \Delta\omega_3^e/\Delta x_1$, which in turns give rise to an edge dislocation density field α_{13}. Remembering that $\alpha_{ij} = b_i t_j$, where b_i is the areal density of Burgers vector along direction $\mathbf{e_i}$ and t_j is the component of line vector along $\mathbf{e_j}$, the component α_{13} obtained for this tilt boundary renders a wall of edge dislocations with straight lines along the tilt axis direction and with Burgers perpendicular to the grain boundary. This is in agreement with the conventional interpretation of tilt boundaries as arrays of edge dislocations. We note that the Burgers vector associated with this mesoscale edge polar

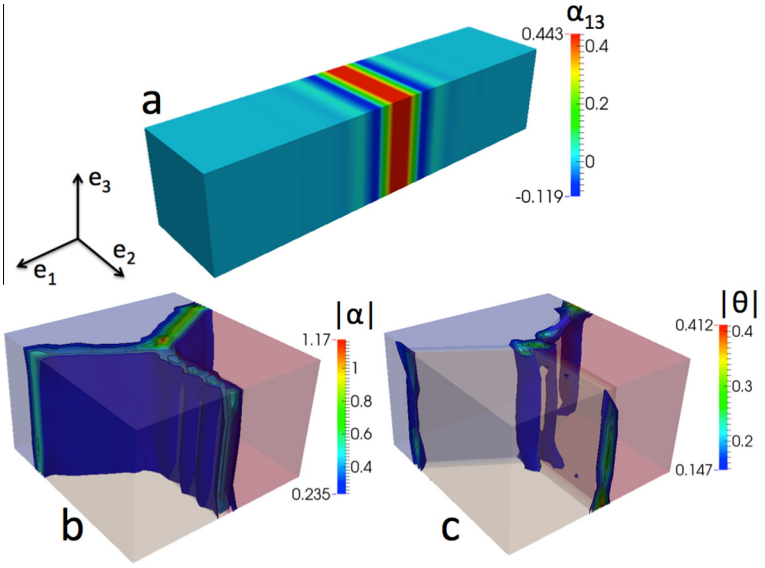

Fig. 2. Initial polar defect densities in mesoscale bicrystals and tricrystals, as estimated from crystal lattice orientations. (a) Edge dislocation density α_{13} (in rad μm^{-1}) in a $20 \times 5 \times 5$ μm^3 bicrystal with a tilt misorientation of 25° around $\mathbf{e}_3$ axis. Periodic boundary conditions are assumed along the GB plane ($\mathbf{e}_2, \mathbf{e}_3$). (b) Norm of the dislocation density tensor (in rad μm^{-1}) in a $15 \times 15 \times 10$ μm^3 tricrystal. The orientation of the three grains are randomly generated such that the grain boundaries have both tilt and twist components. c: norm of the disclination density tensor (in rad μm^{-2}) in the same tricrystal.

dislocation density field is equivalent to that induced by the wedge disclination dipole structure of this same tilt boundary at nanoscale. Hence, the vectorial characteristics of the incompatibility is conserved through the length scales.

3.4. Grain boundaries viewed as interfaces

As already mentionned, the mesocale description of the GBs cannot account for their core structure because they are viewed as a singular interfaces where the field variables may encounter discontinuities. However the jumps of the elastic/plastic strain and cuvature tensor fields across the interface cannot be arbitrary for the consistency of the continuum theory. As recalled below, tangential continuity conditions on the elastic/plastic strain and curvature tensor fields must be satisfied in a framework based on non-singular disclination and dislocation density fields (Acharya, 2007; Fressengeas et al., 2012). Fig. 3 represents a closed circuit C crossing two grains, separated by a singular GB interface (I) of unit normal $\mathbf{n}$ at point P. $\mathbf{l}$ and $\mathbf{t} = \mathbf{n} \times \mathbf{l}$ are unit vectors belonging to the interface, forming an orthonormal basis with $\mathbf{n}$.

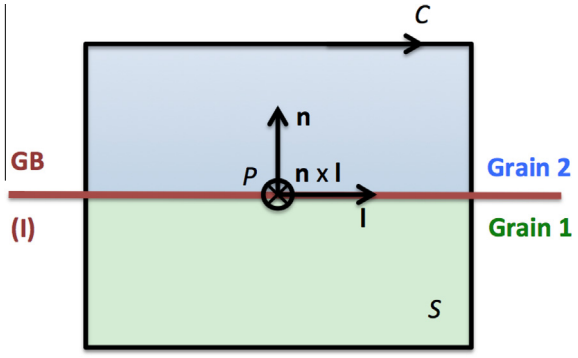

Fig. 3. Mathematical setup used to derive tangential continuity conditions at singular grain boundary interfaces (Acharya, 2007; Fressengeas et al., 2012). Two grains are delimited by a singular GB interface (I) of unit normal $\mathbf{n}$ at point P. The unit vectors $\mathbf{l}$ and $\mathbf{n} \times \mathbf{l}$ belong to the GB plane. A closed circuit C crosses both grains and the GB.

We assume the existence of continuous polar defect densities $(\boldsymbol{\theta}, \boldsymbol{\alpha})$ in both grains and, provisionally, possible surface (singular) defect densities $(\boldsymbol{\theta}^S(I), \boldsymbol{\alpha}^S(I))$ lying in the interface. The Frank and Burgers vectors associated with circuit C can be obtained from Eqs. (21) and (22). When collapsing circuit C onto point P in the interface, Eqs. (21) and (22) become (Fressengeas et al., 2012):

$$[\boldsymbol{\kappa}_e] \cdot \mathbf{l} = \boldsymbol{\theta}^S(I) \cdot \mathbf{t}, \tag{29}$$

$$[\boldsymbol{\epsilon}_e - \boldsymbol{\kappa}_e \times \mathbf{r_0}] \cdot \mathbf{l} = (\boldsymbol{\alpha}^S(I) - \boldsymbol{\theta}^S(I) \times \mathbf{r_0}) \cdot \mathbf{t}, \tag{30}$$

The above equations can be seen as generalized Frank–Bilby interfacial relations applied to both dislocations and disclinations (Frank, 1950; Bilby, 1955). Eq. (29) means that any tangential discontinuity of elastic curvature across the interface can be accommodated by a singular surface disclination density $\boldsymbol{\theta}^S(I)$ lying in the interface. Similarly, Eq. (30) means that any tangential discontinuity of the elastic strain across the interface, including a possible contribution of elastic curvatures and surface disclinations, can be accommodated by a singular surface dislocation density $\boldsymbol{\alpha}^S(I)$ lying in the interface. When disclinations are overlooked, the latter relation reduces to:

$$[\mathbf{U}_e] \cdot \mathbf{l} = \boldsymbol{\alpha}^S(I) \cdot \mathbf{t}, \tag{31}$$

which means that any tangential discontinuity of the elastic distortion across the interface can be accommodated by a singular surface dislocation density $\boldsymbol{\alpha}^S(I)$ lying in the interface (Acharya, 2007). If modeling choices are such that surface defect densities are not allowed, for consistency of the continuous framework, Eqs. (29) and (30) reduce to (Fressengeas et al., 2012):

$$[\boldsymbol{\kappa}_e] \cdot \mathbf{l} = 0, \tag{32}$$

$$[\boldsymbol{\epsilon}_e - \boldsymbol{\kappa}_e \times \mathbf{r_0}] \cdot \mathbf{l} = 0. \tag{33}$$

Eqs. (32) and (33) imply tangential continuity of the elastic curvature and strain tensors across the interface. Similar continuity conditions also apply to the plastic curvature and strain tensors, and the plastic curvature rate and strain rate tensors. Through the limits imposed to the accommodation of discontinuities, non-locality of elasto-plasticity is induced across the interface. The characteristic

length scale of such non-locality is extremely small. Nevertheless, it has a strong impact on the plastic strain rate and rotation rate fields in the vicinity of the grain boundaries, and it allows retrieving size effects on plasticity, loading path-dependency and directional hardening in particle-reinforced alloys, as well as texture peculiarities due to grain interactions (Mach et al., 2010; Richeton et al., 2011; Puri et al., 2011; Taupin et al., 2012). In the forthcoming simulations, we thus propose to investigate further the effects of the interfacial tangential continuity conditions on the predictions of the mesoscale model, in terms of polar defect density distributions at grain boundaries and triple lines, plasticity, material hardening and size effects.

3.5. Elasticity

In the absence of body forces, the momentum and moment of momentum equations reduce to (Mindlin and Tiersten, 1962; Taupin et al., 2014):

$$\mathbf{div}\,\mathbf{T}^{sym} + \frac{1}{2}\mathbf{curl}\,\mathbf{div}\,\mathbf{M}^{dev} = 0. \tag{34}$$

In the above, $\mathbf{T}^{sym}$ and $\mathbf{M}^{dev}$ denote the symmetric Cauchy stress tensor and the deviatoric part of the couple stress tensor, respectively. A specific free energy density function ψ containing contributions from elastic strains and curvatures is now introduced as follows:

$$\psi = \psi(\boldsymbol{\epsilon}_e, \boldsymbol{\kappa}_e). \tag{35}$$

For a quadratic expansion of the latter, the elastic constitutive relations for $\mathbf{T}^{sym}$ and $\mathbf{M}^{dev}$ are derived in the linear form:

$$\mathbf{T}^{sym} = \mathbf{C} : \boldsymbol{\epsilon}_e + \mathbf{D} : \boldsymbol{\kappa}_e, \tag{36}$$

$$\mathbf{M}^{dev} = \mathbf{A} : \boldsymbol{\kappa}_e + \mathbf{B} : \boldsymbol{\epsilon}_e, \tag{37}$$

where the **B** and **D** tensors of elastic constants are non-zero only in defected areas (Upadhyay et al., 2013). Hence, they will be considered as null at mesoscale. Homogeneous and isotropic elasticity is assumed for **C** and the couple stress tensor is taken in the form $\mathbf{M}^{dev} = \xi\mu b^2\boldsymbol{\kappa}_e^{dev}$, where μ and b denote the shear modulus and the magnitude of the Burgers vector, respectively. ξ is a non-dimensional parameter whose value and scale dependence will be discussed in the following.

3.6. Plasticity and scale dependence

To derive a mesoscale measure of plasticity by dislocation glide, we use a space–time running average of the nano-scale plastic strain rate tensor:

$$\dot{\boldsymbol{\epsilon}}_p = (\boldsymbol{\alpha} \times \mathbf{V}_\alpha)^{sym}, \tag{38}$$

where $\mathbf{V}_\alpha$ denotes the velocity of an infinitesimal part of a dislocation. With provisional overbars for the mesoscopic averages, we obtain:

$$\overline{\dot{\boldsymbol{\epsilon}}_p} = (\overline{\boldsymbol{\alpha}} \times \overline{\mathbf{V}_\alpha} + \mathbf{L_p})^{sym}, \tag{39}$$

where $\mathbf{L_p}$ is defined as

$$\mathbf{L_p} = \overline{(\boldsymbol{\alpha} - \overline{\boldsymbol{\alpha}}) \times \mathbf{V}_\alpha} = \overline{\boldsymbol{\alpha} \times \mathbf{V}_\alpha} - \overline{\boldsymbol{\alpha}} \times \bar{\mathbf{V}}_\alpha. \tag{40}$$

Hence, $\mathbf{L_p}$ represents a part of the average plastic distortion rate produced by the nanoscale dislocation density. It can be non-vanishing when $\overline{\boldsymbol{\alpha}} = 0$ and, as such, is to be interpreted as the plastic distortion rate produced by the so-called statistical dislocations (Acharya and Roy, 2006). Clearly, the velocity $\bar{\mathbf{V}}_\alpha$ is a space–time average of the point-wise, nanoscale dislocation velocities $\mathbf{V}_\alpha$. $\bar{\mathbf{V}}_\alpha$ and $\mathbf{L_p}$ are terms that require constitutive specification, to be provided below. Dropping the overbars, the polar dislocation densities are set into motion by the driving force:

$$\mathbf{F}^\alpha = \mathbf{b} - \left(\mathbf{b} \cdot \frac{\mathbf{a}}{|\mathbf{a}|}\right)\frac{\mathbf{a}}{|\mathbf{a}|}, \tag{41}$$

where $\mathbf{b} = \mathbf{T}^{sym}.\boldsymbol{\alpha} : \mathbf{X}$ and $\mathbf{a} = \frac{1}{3}T_{kk}\boldsymbol{\alpha} : \mathbf{X}$. The dislocation velocity is then related to the driving force $\mathbf{F}^\alpha$ by assuming a mobility law ensuring positiveness of the dissipation. The following power law form:

$$V_l^\alpha = v_0^\alpha\left(\frac{T^{VM}}{T_0}\right)^{n_\alpha}\frac{F_l^\alpha}{|F^\alpha|} \tag{42}$$

is often used. In this expression, (v_0^α, T_0) are reference velocity and stress values respectively. T^{VM} denotes the Von Mises stress. Eq. (42) reflects a thermally activated mechanism for high values of the exponent n_α and viscous mechanisms when $n_\alpha \approx 0$. The relationship (41) and (42) is sufficient to ensure incompressibility of plastic straining, by forbidding out of plane motion of edge dislocations, such as climb or cross-slip, whereas the motion of screw dislocations remains unrestricted (Fressengeas et al., 2011). In crystal plasticity, $\mathbf{L_p}$ is the conventional plastic slip rate tensor, which reads:

$$\mathbf{L_p} = \sum_s \dot{\gamma}_s^p \mathbf{m_s} \otimes \mathbf{n_s} = \sum_s \dot{\gamma}_s^p P_s, \tag{43}$$

if $\dot{\gamma}_s^p$ is the plastic slip rate on slip plane s of slip direction $\mathbf{m_s}$ and normal $\mathbf{n_s}$. $\mathbf{P_s}$ is the orientation Schmid tensor. Plastic slip on system s is activated by the resolved shear stress $\tau_s = \mathbf{T} : \mathbf{P_s}$ through the relation:

$$\dot{\gamma}_s^p = \dot{\gamma}_0^p(|\tau_s/\tau_0|)^{n^\alpha} sign(\tau_s), \tag{44}$$

where $\dot{\gamma}_0^p, \tau_0$ and n are the reference plastic strain rate, shear stress and power law exponent, respectively. Well established standard crystal plasticity representations are therefore included in the present mesoscale model.

In a similar manner, using space–time running averages of the nanoscale disclination density tensor, disclination velocity $\mathbf{V}_\theta$ and plastic curvature rate tensor $\dot{\boldsymbol{\kappa}}_p$, allows writing the mesoscopic plastic curvature rate as:

$$\overline{\dot{\boldsymbol{\kappa}}_p} = \overline{\boldsymbol{\theta} \times \mathbf{V}_\theta} = \overline{\boldsymbol{\theta}} \times \overline{\mathbf{V}_\theta} + \dot{\boldsymbol{\kappa}}_p^*. \tag{45}$$

The mesoscopic plastic curvature rate $\overline{\dot{\boldsymbol{\kappa}}_p}$ may be non-zero when the net polarity of a disclination ensemble vanishes at mesoscale: $(\overline{\boldsymbol{\theta}} = 0)$, as for instance in the large circuit shown in Fig. 1(b). In such as case, it becomes:

$$\overline{\dot{\boldsymbol{\kappa}}_p} = \overline{\boldsymbol{\theta} \times \mathbf{V}_\theta} = \dot{\boldsymbol{\kappa}}_p^*. \tag{46}$$

Dropping the overbars, it will be written as:

$$\dot{\boldsymbol{\kappa}}_p = \boldsymbol{\theta} \times \mathbf{V}_\theta + \dot{\boldsymbol{\kappa}}_p^*. \tag{47}$$

We refer to $\dot{\boldsymbol{\kappa}}_p^*$ as the statistical plastic curvature rate. Like $\mathbf{V}_\theta$, it requires constitutive specification, to be provided below and in the next section. Eq. (47) accounts for plasticity processes in relation with the mobility of disclinations, which cannot be described by a pure dislocation-based model. Such processes include the relaxation of elastic curvatures by grain boundary misorientation variation following the motion of GB disclination densities and the concurrent nucleation of GB dislocation densities. Note here that a plastic curvature rate similar to $\dot{\boldsymbol{\kappa}}_p^*$ was proposed by Romanov and Vladimirov (1992) to account for the relaxation of couple stresses by GB rotation.

The motion of polar disclination densities is driven by a Peach-Köhler-type force $\mathbf{F}_\theta$, which writes (Fressengeas et al., 2011):

$$\mathbf{F}_\theta = \mathbf{M}^t \cdot \boldsymbol{\theta} : \mathbf{X}; \quad F_l^\theta = e_{jkl} M_{ij} \theta_{ik}. \tag{48}$$

We propose that the disclination velocity be related to this driving force by the following power law relationship:

$$V_l^\theta = v_0^\theta \left(\frac{M^{VM}}{M_0} \right)^{n_\theta} \frac{F_l^\theta}{|F^\theta|}, \tag{49}$$

in analogy with Eq. (42). In the above expression, (v_0^θ, M_0) are reference velocity and couple stress values, respectively. M^{VM} denotes the Von Mises couple stress. The exponent n_θ reflects thermally activated mechanisms for high values and viscous mechanisms for $n_\theta \approx 0$. It is not necessarily equal to n_α.

When considering statistical plastic strain and curvature rates at mesoscale, the transport equations for polar defect densities (Fressengeas et al., 2011) read:

$$\dot{\boldsymbol{\theta}} = -\mathbf{curl}(\boldsymbol{\theta} \times \mathbf{V}_\theta + \dot{\boldsymbol{\kappa}}_p^*), \tag{50}$$

$$\dot{\boldsymbol{\alpha}} = -\mathbf{curl}(\boldsymbol{\alpha} \times \mathbf{V}_\alpha + L_p)^{sym} + \dot{\boldsymbol{\kappa}}_p^t - tr(\dot{\boldsymbol{\kappa}}_p)\mathbf{I}. \tag{51}$$

The above equations are of the form:

$$\dot{\boldsymbol{\theta}} = -\mathbf{curl}(\boldsymbol{\theta} \times \mathbf{V}_\theta) + \mathbf{s}_\theta^\kappa, \tag{52}$$

$$\dot{\boldsymbol{\alpha}} = -\mathbf{curl}(\boldsymbol{\alpha} \times \mathbf{V}_\alpha)^{sym} + \mathbf{s}_\alpha^\epsilon + \mathbf{s}_\alpha^\kappa. \tag{53}$$

where the disclination and dislocation sink/source terms $\mathbf{s}_\theta^\kappa$ and $(\mathbf{s}_\alpha^\kappa, \mathbf{s}_\alpha^\epsilon)$ are evidenced. Incompatibility of the plastic curvature rate at grain boundaries and triple nodes is expected to generate polar disclination densities $\boldsymbol{\theta}$ through the term $\mathbf{s}_\theta^\kappa$ in Eq. (52). Interestingly, this disclination sink/source term is not present in the nanoscale version of the model (FDDM), where only a dislocation sink/source term arises from the motion of the existing disclinations. Concurrently, plastic curvature rates and incompatibility in the plastic slip rate tensor generate polar dislocation densities $\boldsymbol{\alpha}$ through the terms $\mathbf{s}_\alpha^\kappa$ and $\mathbf{s}_\alpha^\epsilon$ in Eq. (53), respectively. The terms $\mathbf{s}_\alpha^\kappa$ and $\mathbf{s}_\theta^\kappa$ provide new disclination-mediated plastic relaxation mechanisms for grain boundaries, such as dislocation nucleation or absorption (Tschopp et al., 2007; Van Swygenhoven et al., 2006), emergence of disclination lines at triple/quadruple junctions (Rösner et al., 2011), that the pure dislocation version of the model can not render. The predictive capability brought by such sink/source terms will be investigated in the next section.

4. Mesoscale plastic curvature rate, scale dependence and disclination-mediated GB mechanisms

4.1. Expression for the statistical plastic curvature rate

In this subsection, we aim at deriving an expression of the statistical plastic curvature rate $\dot{\boldsymbol{\kappa}}_p^*$ as the average over a mesoscopic volume element of the nanoscale polarized plastic curvature rate $\dot{\boldsymbol{\kappa}}_p = \boldsymbol{\theta} \times \mathbf{V}_\theta$ (see Eq. (46)). In component form, the latter writes:

$$\dot{\kappa}_{ij}^p = \frac{1}{B^\theta} e_{jkl} e_{pql} M_{rp} \theta_{rq} \theta_{ik}, \tag{54}$$

where, using Eq. (49), B^θ denotes the drag coefficient:

$$B^\theta = \frac{|F^\theta|}{v_0^\theta} \left(\frac{M_0}{M^{VM}} \right)^{n_\theta}. \tag{55}$$

Some manipulations allow rewriting Eq. (54) as:

$$\dot{\kappa}_{ij}^p = \frac{1}{B^\theta} \theta_{ik} (\theta_{kl}^t M_{lj} - M_{kl}^t \theta_{lj}); \quad \dot{\boldsymbol{\kappa}}^p = \frac{1}{B^\theta} \boldsymbol{\theta} \cdot (\boldsymbol{\theta}^t \cdot \mathbf{M} - \boldsymbol{\theta} \cdot \mathbf{M}^t). \tag{56}$$

Now, breaking $\theta_{ij} = \Omega_i t_j$ into the Frank vectors around axis $\mathbf{e}_i$ per unit surface, Ω_i, and the component of disclination line along direction $\mathbf{e}_j, t_j$, Eq. (56) can be written in the form:

$$\dot{\boldsymbol{\kappa}}^p = \mathbf{P}^\theta : \mathbf{M}; \quad P_{ijkl}^\theta = \frac{1}{B^\theta} \Omega_i \Omega_k (\delta_{jl} - t_j t_l). \tag{57}$$

In Eq. (57), $\mathbf{P}^\theta$ contains information on the crystallography of grain boundaries in terms of disclinations, as well as on mobility of the latter. Such information is important as it directly controls the capability of grain boundaries to relax elastic curvatures. Future work on this model includes determination of $\mathbf{P}^\theta$ as a function of grain boundary nature, material, temperature etc. Using Eq. (55) for the drag coefficient B^θ, we obtain the statistical plastic curvature rate as:

$$\dot{\kappa}_{ij}^{p*} = \frac{1}{V} \int_V \frac{v_0^\theta}{|F^\theta|} \left(\frac{M^{VM}}{M_0} \right)^{n_\theta} \Omega_i \Omega_k (\delta_{jl} - t_j t_l) M_{kl} dV. \tag{58}$$

Assuming V to be large enough to contain a statistical distribution of the Frank vector and disclination line orientations, we reduce this expression to:

$$\dot{\kappa}_{ij}^{p*} = \frac{1}{V} \int_V \frac{v_0^\theta}{|F^\theta|} \left(\frac{M^{VM}}{M_0} \right)^{n_\theta} \eta^2 \Omega^2 \delta_{ik} \delta_{jl} M_{kl} dV, \tag{59}$$

where Ω is a characteristic Frank vector and η a non-dimensional parameter, and finally obtain:

$$\dot{\kappa}_{ij}^{p*} = \frac{1}{V} \int_V \dot{\kappa}_0^p (M^{VM}/M_0)^{n^\theta} (M_{ij}^{dev}/M^{VM}) dV. \tag{60}$$

For the sake of simplicity, $\dot{\kappa}_0^p = \eta^2 \Omega^2 v_0^\theta M^{VM}/|F^\theta| = \rho \Omega v_0^\theta$ is taken as a constant. $\rho\Omega$ represents a statistical disclination density in units of a characteristic Frank vector times a length of disclination line per unit volume (rad m^{-2}). Note the similarity of this relationship with the conventional Orowan's law for the plastic strain rate resulting from a statistically distributed ensemble of dislocations. Invoking the mean value theorem, the mesoscale plastic curvature rate is finally approximated as follows:

$$\dot{\boldsymbol{\kappa}}_p^* = \dot{\kappa}_0^p (M^{VM}/M_0)^{n^\theta} (\mathbf{M}^{dev}/M^{VM}). \tag{61}$$

Identification of constitutive parameters and scale dependences in the statistical plastic curvature rate (61) is performed in the next subsection.

4.2. Scale dependence of curvatures and constitutive parameters

In the presence of a discontinuity of the elastic/plastic rotation at a GB interface, the elastic/plastic curvatures across the interface are scale dependent, meaning that their values depend on the choice of the resolution length scale. Clearly, they are inversely proportional to the resolution length scale. Hence, the question arises as to what should be the scale dependence of the constitutive parameters to ensure the conservation through the resolution length scales of the GB energy and dissipated energy in a GB-mediated plasticity process. Put differently, we look for scaling laws such that the GB elastic energy and GB-mediated plasticity mechanisms modeled smoothly at nanoscale via fields of polar disclination densities, be rendered consistently at mesoscale when using sharp interfaces and curvatures defined in an averaged sense. To illustrate this point, we simulate the bending of a bicrystal containing a symmetric tilt boundary with various resolution length scales, as shown in Fig. 4. The configuration of the bicrystal is sketched at the top of the figure. The tilt axis is perpendicular to the figure and the tilt angle is indicated by two dashed lines. A typical high angle $\langle 001 \rangle \Sigma 5(310)$ tilt boundary of misorientation 36.9° is considered. The mechanical behavior of each crystal is taken as purely elastic. In addition the crystals are dislocation free, so that any plastic distortion of the bicrystal is produced via GB mechanims. A constant and uniform bending curvature is then applied to

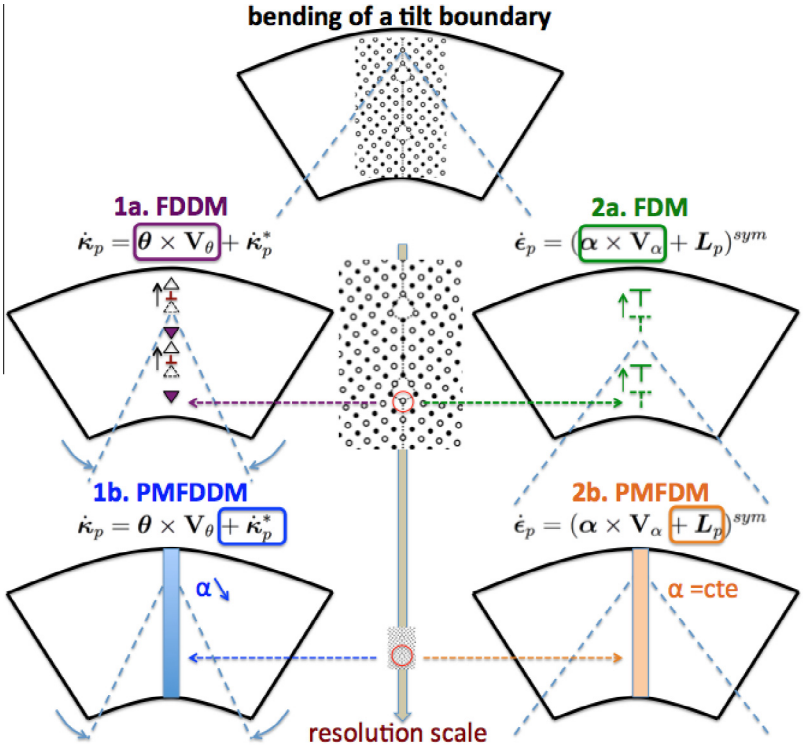

Fig. 4. Bending of a bicrystal containing a symmetric tilt GB. The configuration of the bicrystal is shown on top. The two crystals are supposed purely elastic and do not contain any defect. The tilt boundary rotation axis is perpendicular to the figure and the GB is represented by its atomic structure featuring structural units. The GB misorientation is indicated by the two dashed lines. A constant and uniform bending curvature is applied to the bicrystal, such that the left and right external surfaces are at a 10° angle. Results from simulations of this configuration at nanoscale with FDDM (Case 1a) and FDM (Case 2a) and at mesoscopic scale with PMFDDM (Case 1b) and PMFDM (Case 2b) are sketched below. See the main text for explanations.

the bicrystal, such that the left and right external surfaces are at an angle of 10°.

We first perform a reference simulation at nanoscale (Case 1a), as sketched in Fig. 4(1a). In this simulation, FDDM is used. The simulation parameters are listed in Table 1. The resolution length scale, *i.e.* the mesh size in the finite element simulation, is $l_0 = 0.1$ nm, a value taken as reference. The structural units composing the tilt boundary at nanoscale are modeled smoothly via dipoles of wedge disclination densities, as done in previous work (Fressengeas et al., 2014). The corresponding initial energy of the GB (excess energy per unit length of GB) is $E_{gb}(l_0) = 1\ \mathrm{J/m^2}$. This value will be used as a reference in the following. The following mechanism, referred to as grain boundary misorientation variation throughout the present paper, is predicted by the model. Due to the internal elastic fields of the GB disclinations and the imposed bending, strong elastic curvatures exist in the disclination-populated areas along the GB. Their conjugate couple stresses drive the motion of disclinations, as implied by Eqs. (48) and (49). Negative disclinations move up along the boundary plane. From Eqs. (47) and (53), such disclination motion generates positive plastic curvatures and leaves positive polar GB edge dislocations in their wake. The Burgers vector of the generated edge dislocation densities is perpendicular to the GB plane and their line is normal to the figure. As a consequence of the generated plastic curvatures and associated dislocation densities, the strong elastic curvatures in the GB area are relaxed and the GB misorientation decreases by a 10° angle, as suggested by the dashed lines in the figure. Hence, this process can be described as a GB misorientation variation mediated by GB disclination motion and accompanied by GB dislocation nucleation. Thus, in contrast with previous generic considerations on disclinations (Kleman and Friedel, 2008), the crystal is not seen as "suffering" from the motion of disclinations, but rather as being relaxed in this dissipative process. Moreover, the so-called relaxation dislocations (Kleman and Friedel, 2008) produced by the motion of disclinations do not need to move away from the GB. The energy dissipated per unit GB length in reducing the misorientation is calculated as:

$$E_d = \frac{1}{L_{GB}} \int_t \left(\int_V (\mathbf{T} : \dot{\boldsymbol{\epsilon}}_p + \mathbf{M} : \dot{\boldsymbol{\kappa}}_p) dV \right) dt. \tag{62}$$

It is found to be $E_d(l_0) \approx 0.2\ \mathrm{J/m^2}$, which clearly amounts to 20% of the initial GB energy. This value will also be used as a reference for the energy dissipated by the change of misorientation of the tilt boundary in what follows. Other reference parameters to be identified from this simulation are $M_0(l_0)$ and $\dot{\kappa}_0^p(l_0)$. $\dot{\kappa}_0^p(l_0)$ is estimated from the plastic curvature variation due to disclination mobility, divided by the time during which bending is applied. It is found to be $\dot{\kappa}_0^p(l_0) = 10^9\ \mathrm{rad\ m^{-1}\ s^{-1}}$. The reference couple stress is of the form $M_0(l_0) = \xi(l_0)\mu b^2 \kappa_0^e(l_0)$, where $\xi(l_0)$ is the value of the couple stress coefficient in the elastic law $\mathbf{M}^{dev} = \xi \mu b^2 \boldsymbol{\kappa}_e^{dev}$ at resolution length scale l_0. As suggested above, this coefficient must be scale dependent. Its reference value will be $\xi(l_0) = 10^{-10}$ as further detailed below. $\kappa_0^e(l_0)$ reflects a characteristic elastic misorientation over the reference resolution length scale, estimated from the initial

Table 1
Numerical constants used and measured in the reference bending simulations with FDDM.

$n^{\theta,\alpha}$	$\dot{\kappa}_0^p(l_0)$	$\kappa_0^e(l_0)$	T_0	v_0^α
10	10^9 rad m^{-1} s^{-1}	10^9 rad m^{-1}	1 GPa	0.1 nm/s
v_0^θ	E	ν	$\xi(l_0)$	l_0
0.1 nm/s	62.780 GPa	0.3647	10^{-10}	0.1 nm

values of the elastic curvatures within the boundary area. The value $\kappa_0^e(l_0) = 10^9$ rad/m is retained.

We now proceed with simulations at larger resolution length scales l, from the reference scale l_0 up to micron size (Case 1b shown in Fig. 4(1b)). In these simulations, the mesoscopic extension of the FDDM model (to be referred to as PMFDDM: Phenomenological Mesoscale FDDM) is used to model the same bending experiment. As already indicated, we aim at producing results that are consistent with those obtained in Case 1a, by using the mesoscopic plastic curvature rate $\dot{\boldsymbol{\kappa}}_p^*$. The objective is to calibrate the constitutive parameters such that the mesoscopic model quantitatively retrieves the reference GB energy, as well as the misorientation change and the reference energy dissipated in the process. The characteristic resolution length scale (*i.e.* the mesh size) used in the finite element simulations is denoted by l. It was varied from 0.1 nm up to 1 μm. As aforementioned, the initial GB is not rendered by smooth wedge disclinations in these mesoscale simulations, but by a polar edge dislocation density, as implied by Eq. (31). As shown in Fig. 4, the initial tilt boundary supports a uniform wall of negative edge dislocation density with Burgers vector normal to the boundary plane. At nanoscale, where the core structure of GBs is fully captured by wedge disclination dipoles, the initial GB energy is due almost exclusively to elastic strains (Fressengeas et al., 2014). At mesoscale however, where the core structure is overlooked, the initial energy E_{gb} of the GB arises solely from the elastic curvatures and their couple stress conjugates. For the smallest resolution length scale tested ($l = 0.1nm = l_0$), we calibrate the coefficient $\xi = \xi(l_0)$ entering the couple stress elasticity law to ensure that the GB energy equals the reference value obtained with FDDM in Case 1a. The value $\xi(l_0) = 10^{-10}$ is found. Now, we increase l to find the scale dependence of $\xi(l)$ such that the GB energy remains scale independent. We find that $\xi(l)$ and thus the couple stresses should follow the quadratic dependence:

$$\xi(l) = \xi(l_0)\left(\frac{l}{l_0}\right)^2; \quad \mathbf{M}^{dev}(l) = \xi(l_0)\left(\frac{l}{l_0}\right)^2 \mu b^2 \boldsymbol{\kappa}_e^{dev}. \tag{63}$$

As suggested above, this result derives from the scale dependence of the elastic curvatures. Since the jump in elastic/plastic rotation across the interface is invariant when the resolution length scale l is changed, $\kappa_0^e(l)$ and $\dot{\kappa}_0^p(l)$ follow a $1/l$ scaling law:

$$\kappa_0^e(l) = \kappa_0^e(l_0)\frac{l_0}{l}; \quad \dot{\kappa}_0^p(l) = \dot{\kappa}_0^p(l_0)\frac{l_0}{l}. \tag{64}$$

With the identified constitutive parameters and scaling laws, bending simulations are now performed by using the mesoscale model PMFDDM. Due to the applied couple stresses, the statistical plastic curvature rate $\dot{\boldsymbol{\kappa}}_p^*$ generates uniform positive plastic curvatures and positive edge dislocation densities in the interface. Therefore the initial negative dislocation density decreases, as sketched in Fig. 4. Hence, similarly to Case 1a, the GB misorientation decreases, actually by an amount of 6°, in rather good agreement with the reference simulation using nanoscale smooth FDDM in Case 1a. In addition, the energy dissipated during this plastic relaxation process is found to be $E_d = 0.125\ \mathrm{J/m^2}$, also close to the reference value of Case 1a. Simulations at different scale resolutions l show that the dissipated energy is scale independent. All the above results on scale-dependence in the mesoscale bending simulations with PMFDDM are summarized in Fig. 5.

4.3. Disclination vs. dislocation-mediated plasticity at grain boundaries

In this Section, the intent is to show that the pure dislocation version of our model (no disclinations) cannot render mechanisms

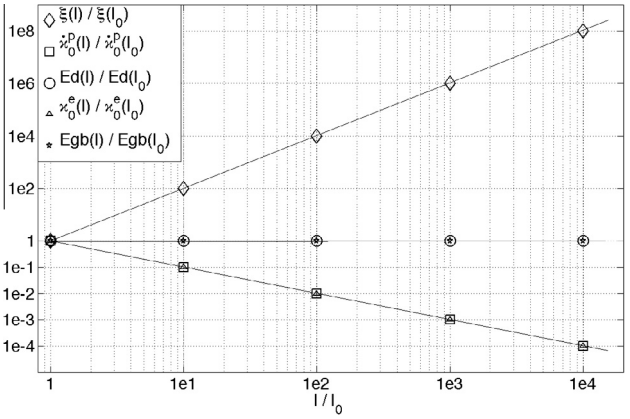

Fig. 5. Log–log plot as a function of resolution length scale l of couple stress elasticity coefficient ξ, reference plastic curvature rate $\dot{\kappa}_0^p$, energy dissipated during GB misorientation change E_d, reference elastic curvature κ_0^e and initial GB energy E_{gb}. Results are normalized by values at reference resolution length scale l_0.

such as the GB misorientation variation presented in the above subsection, in order to make clear that the mesoscale term $\dot{\boldsymbol{\kappa}}_p^*$ effectively adds new plasticity mechanisms to more conventional models relying only on dislocation glide. To this end, two different simulations were performed, which are sketched in Fig. 4(2a) and (2b). In the Case 2a, FDM (Field Dislocation Mechanics) was used to model the tilt boundary at nanoscale with resolution length $l = l_0 = 0.1$ nm. In this case, each atomic structural unit is modeled by a negative edge polar dislocation density spot, with Burgers vector perpendicular to the GB plane and line vector parallel to the tilt axis. If climb is allowed, the edge dislocation can move up or down along the GB, depending on whether they are located in a region of tension or compression. However, such motion does not relax the bending curvatures and the GB misorientation is quasi-invariant. In Case 2b, the tilt boundary is modeled at micron scale ($l = 1$ μm) using PMFDM. Here, as in PMFDDM simulations, the initial GB is composed of a uniform wall of negative edge polar dislocation density. Transport of the polar dislocation density by climb is also possible, as in Case 1a, but no plastic curvature is produced and the GB misorientation does not change. To summarize, our simulations clearly show that disclination motion provides unconventional plastic relaxation mechanisms at GBs, such as GB misorientation variation accompanied by GB dislocation nucleation, that cannot be rendered by dislocation models. Further, these mechanisms can be described by both nanoscale and mesoscale disclination-based models.

5. Mesoscale simulations of bicrystals and tricrystals

5.1. Simulation details

In this section, illustrative applications of the PMFDDM approach are presented. Aluminum bi- and tri-crystals are used as supporting configurations. The intent is to probe the impact of the tangential continuity conditions on elastic/plastic strain/curvature and strain/curvature rates at the interfaces on the mechanical response of these structures. A particular focus will be on the influence of these tangential continuity conditions on the sample size dependence of the mechanical response. Further, the coupled contributions of polar and statistical defect densities to bulk vs. GB mediated plasticity will be examined, together with the role of triple lines and temperature.

To this end, the field equations of the mesoscale model presented in Sections 3 and 4 are solved approximately by using the

finite element method. The open source software FreeFem++ is used (Hecht et al., 2014). The tangential continuity conditions (32) and (33) are imposed by spreading the GB interface over a finite element (with small but non-zero width), which regularizes the discontinuity. Adding a penalty term to the transport Eqs. (50) and (51) allows ensuring that the nucleation of polar defect densities corresponding to tangential discontinuity does not occur. Then, by correcting the incompatible elastic–plastic strains and curvatures from Eqs. (15) and (20), tangential discontinuity is effectively removed and relations (32) and (33) are satisfied. The material constants representative of pure aluminum are used. For the sake of simplicity, no work hardening is implemented. Parameters used for the dislocation crystal plasticity formulation are $\dot{\gamma}_0^p = 10^{-7}\ s^{-1}$ and $\tau_0 = 10$ MPa. Other parameters are already listed in Table 1.

5.2. Non-local impact of tangential continuity on plasticity

Fig. 6(a) and (b) displays the polar dislocation density and tensile plastic strain generated during tensile deformation of the tricrystal shown in Fig. 2 when the tangential continuity conditions are not imposed. A 1% tensile strain ϵ_{33} is applied along the direction of the triple line, with constant quasi-static applied strain rate. The tensile plastic strain exhibits discontinuities across the GBs. It is quasi-uniform within the grains, and there does not seem to be any grain-to-grain elasto-plastic interaction across the GBs. As a consequence of tangential discontinuity of the plastic straining, the polar dislocation density that is generated is localized in the GB interfaces, as can be seen in Fig. 6(a). Conversely, Fig. 6(c) and (d) shows the results predicted for the same tricrystal when the tangential continuity conditions are imposed. Continuity of the tensile plastic strain, grain-to-grain elasto-plastic interactions and a re-distribution of the plastic strain rate between grains are now seen to occur across the GBs. The grain where the plastic strain was the lowest in the absence of the continuity conditions, now has the largest plastic strain. As shown in Fig. 6(c), this is due to polar dislocation densities piling up at GBs in the neighboring grains, which produces internal stresses leading to intergranular transfer of plastic deformation. Note in Fig. 6(c) the concomitant absence of interface dislocations. Fig. 7 shows the macroscopic tension–compression curves corresponding to the deformation of the tricrystal, with and without tangential continuity conditions. The accumulation of polar dislocations at grain boundaries and the grain-to-grain interactions predicted when the tangential continuity conditions are activated lead to more pronounced Bauschinger effect, and particularly to transient elasto-plastic behavior during load reversal.

Additionnally, the polar disclination densities generated during plastic deformation of the tricrystal, with and without tangential continuity conditions, are shown in Fig. 8. Without tangential continuity, most of the disclination density is localized within the triple line. When continuity conditions are imposed, the disclination density is not restricted anymore to the triple line, but rather accumulated along the triple line and the GBs. As for dislocation densities, tangential continuity of the elastic curvatures tends to remove interface disclinations, in favor of more heterogeneous distributions within grains, near triple line and GBs. It also leads to grain-to-grain interactions of elastic curvatures. Such non-local behavior is expected to generate considerable kinematic hardening in situations involving strong elastic curvatures, such as high accumulation of dislocations at grain boundaries at large strains, and bending or torsion solicitations. One should again note that the nucleation of polar disclination densities within grains and along interfaces stems from the presence of the statistical plastic curvature rate introduced in the above section. The latter is also a source or sink of dislocations in Eq. (51). As aforementioned, a careful validation of this statistical term is needed in future work to quantify its impact on the deformation of polycrystals.

5.3. Long-range and size effects induced by tangential continuity

Fig. 9 now illustrates the effects of sample and grain size induced by the tangential continuity conditions on the distribution of plastic strain in a bicrystal and the mechanical behavior of the latter. In a first step, a reference bicrystal composed of two grains of width $H = 5$ μm and length $L = 5.5$ μm with a symetric tilt boundary of misorientation 10°, is deformed in simple tension to a strain of 10% along the $\mathbf{e}_3$ axis. The prefactor $\dot{\gamma}_0^p$ in the plastic slip rate is divided by a factor 10 in the right hand side grain in order to mimic lower dislocation activity in that grain, and to promote differences in the plastic strain across the GB. Fig. 9(a) depicts the tensile plastic strain field ϵ_{33}^p by the end of the tension process if tangential continuity of the plastic strain and curvature tensors is not required. ϵ_{33}^p is seen to be uniform within the grains, while a

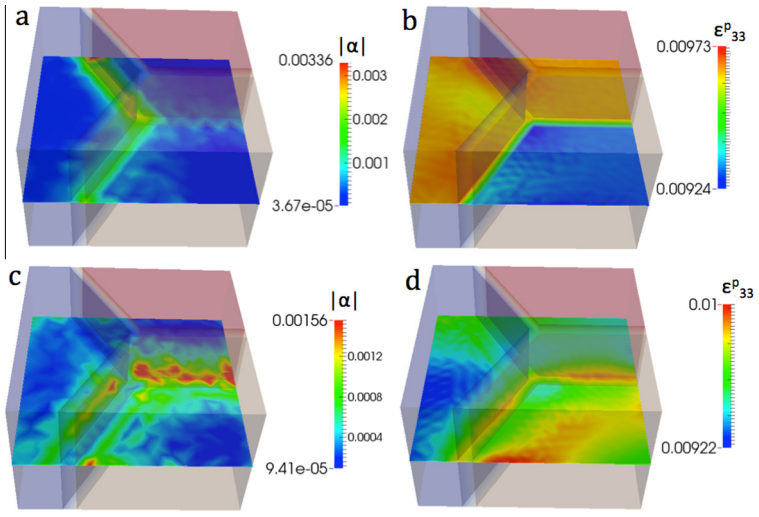

Fig. 6. Tensile deformation of the $15 \times 15 \times 10\ \mu m^3$ tricrystal shown in Fig. 2, without (a), (b) and with (c), (d) tangential continuity conditions. The applied strain is 0.01 along the triple line direction and the applied strain rate is $10^{-5}\ s^{-1}$. (a), (c) Slice showing the norm of the dislocation density tensor (in rad μm^{-1}) generated during plastic deformation. (b), (d) Slice showing the tensile plastic strain at the end of loading.

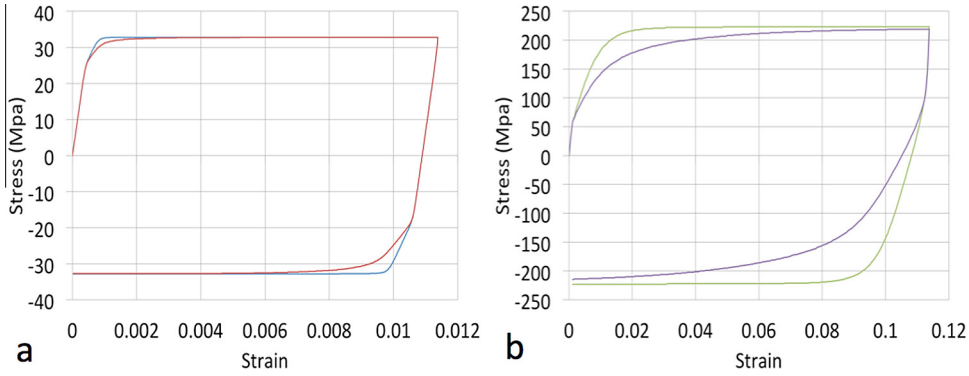

Fig. 7. Tension–compression macroscopic stress–strain curves for the tricrystal shown in Fig. 6. Tension and compression are applied along the triple line direction. (a) Curves obtained with $n^{\alpha} = n^{\theta} = 10$, with (red line) and without (blue line) interface tangential continuity conditions. (b) Curves obtained with $n^{\alpha} = n^{\theta} = 2$, with (purple line) and without (green line) interface tangential continuity conditions. (For interpretation of the references to colour in this figure caption, the reader is referred to the web version of this article.)

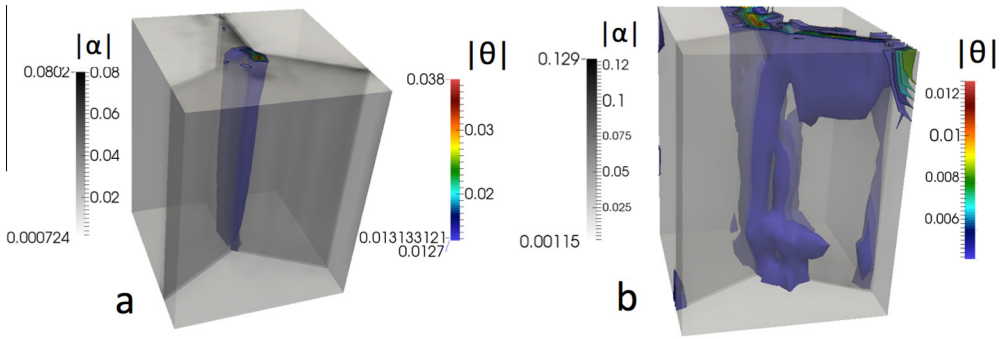

Fig. 8. Compression of a tricrystal, without (a) and with (b) interface tangential continuity conditions. The applied strain is -10% along the triple line direction and the applied strain rate is -10^{-5} s^{-1}. (a), (b) Color contours showing the norm of the disclination density tensor (in rad μm^{-2}) generated during plastic deformation. The norm of the dislocation density tensor generated along the process is shown in gray scale (in rad μm^{-1}).

discontinuity in ϵ^p_{33} shows up across the GB. The configuration of the bicrystal is actually such that tangential continuity of the plastic strain at the interface requires that ϵ^p_{33} be continuous across the interface. This is indeed verified in Fig. 9(b), obtained from calculations where tangential continuity is implemented. In addition, polar dislocation pile-ups build-up at the GB, and slip transfer across GB takes place, similar to that previously shown in Fig. 6. The width of the bicrystal is now doubled from $H = 5$ μm to $2H = 10$ μm, while its length $L = 5.5$ μm is kept constant. The resulting tensile plastic strain field is shown in Fig. 9(c), with tangential continuity still implemented. As compared to Fig. 9(b), it is seen that the heterogeneity of the plastic strain is enhanced, because the amount of GB area is increased. The role of the dislocation pile-ups in slip transfer is also promoted. As a result, more plastic strain is produced in the hard grain on the right. Finally, while maintaining the width of the grains equal to $2H = 10$ μm and keeping tangential continuity in place, their length is now increased to $2L = 11$ μm. The resulting plastic strain field is shown in Fig. 9(d). As compared to Fig. 9(c), it is seen that the effect of slip transfer progressively decreases as one moves away from the GB, while the influence of the boundary conditions on this region decreases. This clearly shows the non-local and long-range character of the effects of tangential continuity on the plastic strain field. The impact of the above changes in size on the stress–strain curves of the bicrystal are shown in Fig. 9(e). For the grains with dimension $2H = 10$ μm and $L = 5.5$ μm, slip transfer is effective in almost all parts of the hard grain, including the vicinity of the external boundaries. Hence, the Bauschinger effect and transient elastoplastic transition during strain reversal are increased. For the grains with dimension $2H = 10$ μm and $2L = 11$ μm, slip transfer is less effective away from the GB. Hence, the Bauschinger effect and transient elastoplastic transition during strain reversal are less pronounced. Importantly, it is to be noted that changing the dimensions of the bicrystal does not have any effect on the plastic strain field and the overall mechanical response when the tangential continuity conditions are not imposed.

5.4. GB vs. dislocation mediated plasticity

We now look for the predictive capabilities of the model in terms of dislocation vs. GB mediated plasticity. Fig. 10 shows the shear deformation of a $20 \times 1 \times 1$ μm^3 bicrystal with a 25° ⟨001⟩ symmetric tilt boundary supporting the appropriate edge dislocation density field. Dislocation glide within grains is possibly prevented by arbitrarily setting $\dot{\gamma}^p_0 = 0$ in the plastic slip rate tensor. Periodic boundary conditions are assumed along the two directions defining the GB plane. Simple shear with constant quasi-static applied strain rate is imposed on the external surfaces parallel to the GB plane. Unsurprisingly, the imposed shear is accommodated by intragranular plastic shear when $\dot{\gamma}^p_0 \neq 0$, as can be seen in Fig. 10(b), where the residual strain after loading removal is shown. If instead intragranular dislocation glide is not permitted: $\dot{\gamma}^p_0 = 0$, the bicrystal behaves elastically until the applied shear stress reaches a critical value where transport of the edge dislocation density decorating the tilt boundary takes place. Accordingly, Fig. 10(c) depicts the occurrence of shear-coupled boundary migration. Further, Fig. 11 shows the predicted shear-coupling factor

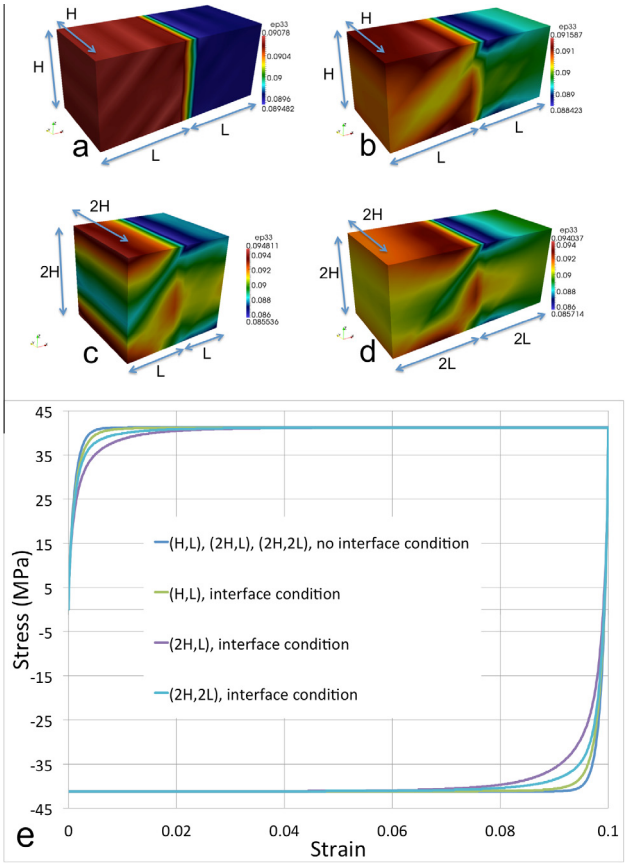

Fig. 9. Grain size effects during tension–compression of a bicrystal. (a) Reference bicrystal of dimension $H = 5$ μm and $L = 5.5$ μm, deformed to a 10% strain in simple tension along $\mathbf{e}_3$ axis (green z axis in the figure), without tangential continuity conditions. The applied strain rate is 10^{-5} s^{-1}. The misorientation of the symetric tilt GB is 10° around the e_3 axis. The prefactor $\dot{\gamma}_0^p = 0$ in the plastic slip rate tensor is divided by a factor 10 in the right grain in order to mimic lower dislocation activity in that grain. (b) Same bicrystal than that shown in a, but tangential continuity conditions are imposed. (c) Same bicrystal than that shown in a, but its width is increased from $H = 5$ μm to $2H = 10$ μm and tangential continuity conditions are imposed. (d) Same bicrystal than that shown in a, but its width is increased from $H = 5$ μm to $2H = 10$ μm, the length of grains are increased from $L = 5.5$ μm to $2L = 11$ μm and tangential continuity conditions are imposed. In (a,b,c,d), the tensile plastic strain is color-coded. (e) Corresponding stress/strain curves of the bicrystal. Without continuity conditions, changing H and/or L yields the same macroscopic curve without any size effect. (For interpretation of the references to color in this figure legend, the reader is referred to the web version of this article.)

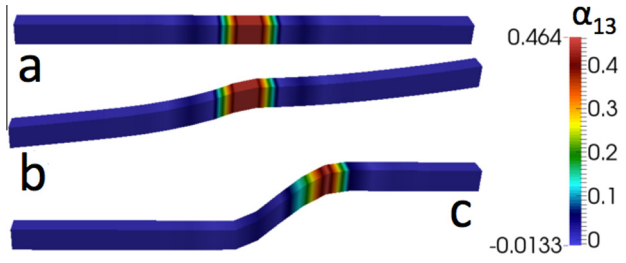

Fig. 10. Shear deformation of a $20 \times 1 \times 1$ μm^3 bicrystal with tilt misorientation of 25°, the tilt axis $\mathbf{e}_3$ is normal to the figure. Periodic boundary conditions are assumed along the GB plane $(\mathbf{e}_1, \mathbf{e}_3)$. (a) Initial edge dislocation density α_{13} (in rad μm^{-1}) composing the tilt GB. (b) Edge dislocation density α_{13} (in rad μm^{-1}) in the same bicrystal deformed by a 15% shear strain. (c) The two crystals are made purely elastic by setting $\dot{\gamma}_0^p = 0$ in the plastic slip rate. In that case, the 15% applied shear strain is accommodated by the motion of the edge dislocation density α_{13} (in rad μm^{-1}), leading to shear-coupled boundary migration. In (b), (c), the deformed shape after removal of the applied shear strain is shown to evidence the residual shear strain in the bicrystal.

when the tilt angle is varied by appropriately choosing the initial GB dislocation density. The experimentally observed positive and negative branches (Gorkaya et al., 2009) are retrieved. The switch between the branches is predicted at a 45° tilt, due to cubic symmetry reasons, whereas the actual value is 37°, as predicted by the nanoscale FDDM model (Taupin et al., 2014) and observed in experiments (Gorkaya et al., 2009). Despite their mesoscale character, which prevents from recovering fine scale features, these results compare favorably with the experimental values. The predicted critical shear stress for boundary migration is also shown in Fig. 11 as a function of the misorientation. It is seen to be high at low angles and conversely low at high angles, consistent with the elastic energy and dislocation content of these boundaries. Indeed, if a constant critical driving force is assumed at all misorientations, Eqs. (41) and (42) show that the higher the GB dislocation density is taken, the lower the shear stress becomes.

5.5. Effect of triple lines and temperature on GB-mediated plasticity

Finally, Fig. 12 shows GB-mediated plasticity in a tricrystal configuration. Again, intragranular slip is prevented by setting $\dot{\gamma}_0^p = 0$ in the plastic slip rate. Periodic boundary conditions are imposed along the triple line direction. The GBs are of tilt/twist character and simple shear is applied on the external surfaces, both along and normal to the triple line direction, in order to activate glide of both the edge and screw polar dislocation densities present in the GBs. The applied strain rates are constant and quasi-static. An initial edge dislocation component of the boundaries is shown in Fig. 12(a). Because of the mixed character of the GBs and the presence of a triple line and free surfaces close to the GBs, the defect dynamics is much more complex than in the bicrystal shown in Fig. 10(c). In particular, it can be seen in Fig. 12(b) that boundary migration is hindered by the presence of the triple line. As a result the applied shear is accommodated by local variations in GB misorientation associated with the nucleation of GB edge and screw dislocations and with their eventual emission in grain interiors. For instance, one of the GBs in Fig. 12(b), essentially of tilt character, encounters a 60% decrease of its tilt angle (a reduction of about 15°), while dislocation emission into a neighbor grain interior is clearly in evidence. The same tricrystal configuration is

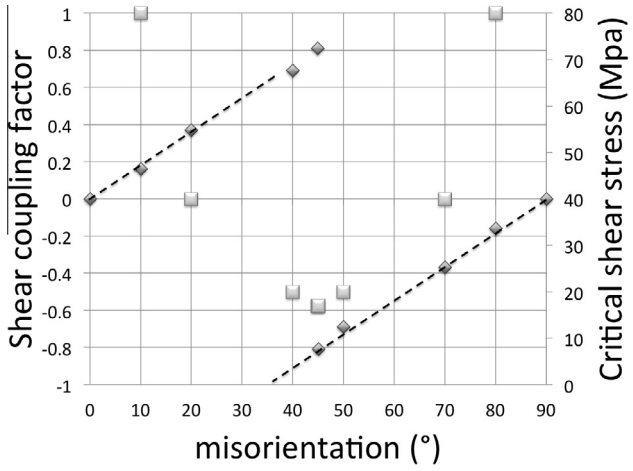

Fig. 11. Shear-coupling factor of ⟨001⟩ tilt boundaries, as predicted by the mesoscale model. Diamonds show the predicted shear-coupling factors, for misorientations ranging from 0 up to 90°. Two positive and negative branches are obtained with a switch at 45° due to cubic symmetry. The two dotted lines represent the two branches obtained experimentally with a switch at 37° (Gorkaya et al., 2009). Squares show the predicted critical shear stress (MPa) for the onset of boundary migration, as a function of misorientation.

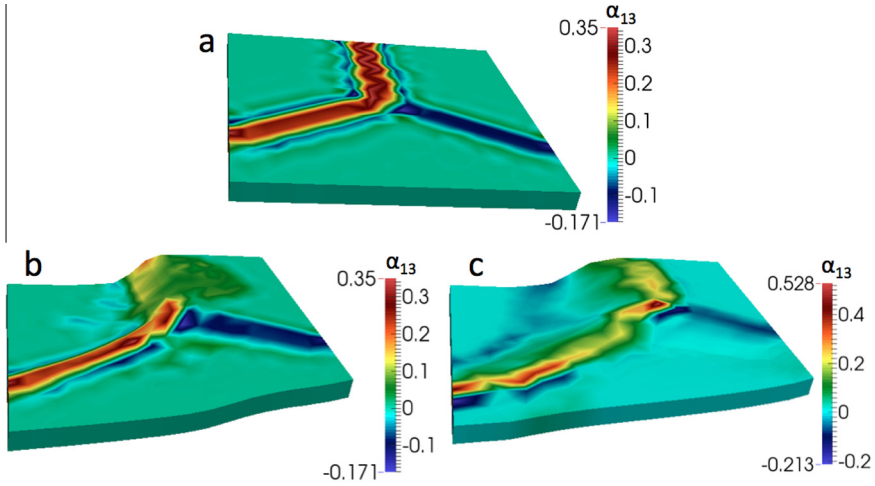

Fig. 12. Deformation of a $15 \times 15 \times 1\ \mu m^3$ tricrystal with three grain boundaries that have each both tilt and twist components. The three grains are made purely elastic by setting $\dot{\gamma}_0^p = 0$ in the plastic slip rate tensor. Periodic boundary conditions are assumed along the triple line direction. (a) Initial edge dislocation density α_{13} (in rad μm^{-1}) decorating part of the grain boundaries. (b) Evolution of the dislocation density α_{13} (in rad μm^{-1}) when a 15% shear strain is applied normal and along the triple line direction, with $n^\alpha = n^\theta = 10$. The triple line and grain boundaries are almost motionless. The upper GB has accommodated deformation by emitting edge dislocations to its right and by consequently decreasing its tilt misorientation by 60% locally. (c) Evolution of the dislocation density α_{13} (in rad μm^{-1}) when a 15% shear strain is applied normal and along the triple line direction, with $n^\alpha = n^\theta = 1$. A 15% tensile strain is also applied normal to the triple line to promote out-of-plane motion of polar edge dislocations. Climb and glide of edge dislocations are treated on an equal footing. In that case, the triple line and grain boundaries migrate to accommodate deformation.

looked at in Fig. 12(c) when additional tension is applied along a direction normal to the triple line, in order to favor climb of edge dislocations. In addition, the power law exponents are set to $n^\alpha = n^\theta = 1$ in the mobility laws (42) and (49), in order to mimic viscous motion of defects at high temperature. Climb of edge dislocations is also allowed. As can be seen in Fig. 12(c), GB migration is substituted to the grain boundary misorientation variation mechanism and to dislocation nucleation and emission. To summarize, these simulations suggest that viscosity and dislocation climb tend to favor GB migration, whereas GB misorientation variations and dislocation nucleation and emission tend to prevail when the strength of the obstacles increases.

6. Conclusions

In the present paper, a mesoscale extension of a previously developped elasto-plastic theory of dislocation and disclination fields has been introduced. The approach is useful in polycrystalline materials where plasticity by dislocation glide is limited, either because the average grain size becomes too small, as in ultrafine-grained materials, or because the material does not have enough independent slip systems, as in orthorhombic olivine. Motivated by recent experimental results (Beausir and Fressengeas, 2013), where mesoscale disclination dipoles were found to decorate GBs and triple lines, the tensorial densities of crystal defects (dislocations and disclinations) are used to render continuously the initial structure of the GBs and triple lines. Their transport provides the framework for the dynamics of the GBs and triple lines. Consistency of the latter in the coarse-graining process requires introducing a statistical plastic curvature rate tensor, whose role is to reproduce GB-mediated plasticity at mesoscale. Appended with tangential continuity conditions on the plastic strain and curvature rate tensors at GBs, the theory offers a nonlocal description of the plasticity of polycrystals. Nonlocality arises at GBs and triple lines, and has long-range character. Predicted consequences of non-locality include the occurrence of pile-ups of dislocation densities at GBs and activation of slip across GBs, interactions between neighbor grains, sample and grain size effects on mechanical behavior, anisotropy of hardening induced by the loading process ("kinematic" or directional hardening), GB migration and misorientation variation accompanied with dislocation nucleation and emission,etc. Standard crystal plasticity is included in the theory as a limiting case, when the crystal defect density fields and the statistical plastic curvature rate vanish and when the tangential continuity conditions on the plastic strain and curvature rate tensors are overlooked at GBs. The above nonlocal features are naturally obtained by the theory, without introducing any *ad hoc* phenomenological term. As a challenge for future work, the approach has in particular the capacity for predicting the influence of grain size on the work hardening of polycrystals, as a function of temperature and strain rate.

Acknowledgements

The authors benefited of financial support from the ANR (Agence Nationale de la Recherche) under Grant ANR-11-JS09-007-01, NanoMec. The authors would like to thank A. J. Beaudoin, S. Forest and R. Lebensohn for helpful discussions.

References

Acharya, A., 2001. J. Mech. Phys. Solids 49, 761.
Acharya, A., 2007. Philos. Mag. 87, 1349.
Acharya, A., Roy, A., 2006. J. Mech. Phys. Solids 54, 1687.
Beausir, B., Fressengeas, C., 2013. Int. J. Solids. Struct. 50, 137–146.
Bozhko, S.I., Taupin, V., Lebyodkin, M., Fressengeas, C., Levchenko, E.A., Radikan, K., Lübben, O., Semenov, V.N., Shvets, I.V., 2014. Phys. Rev. B 90, 214106.
Bilby, B.A., 1955. In: Bristol Conference Report on Defects in Crystalline Solids, The Physical Society, London, 124.
Bitzek, E., Derlet, P.M., Anderson, P.M., Van Swygenhoven, H., 2008. Acta Mater. 56, 4846.
Bollmann, W., 1970. Crystal Defects and Crystalline Interfaces. Springer-Verlag.
Cahn, J.W., Mishin, Y., Suzuki, A., 2006. Acta Mater. 54, 4953.
Cordier, P., Demouchy, S., Beausir, B., Taupin, V., Barou, F., Fressengeas, C., 2014. Nature 507, 51–56.
deWit, R., 1970. In: Simmons, J.A., deWit, R., Bullough, R. (Eds.), Fundamental Aspects of Dislocation Model, vol. I. Nat. Bur. Stand. (US), Spec. Publ. 317, pp. 651–673.
Farkas, D., Froseth, A., Van Swygenhoven, H., 2006. Scr. Mater. 55, 695–698.
Frank, F.C., 1950. In: Symposium on The Plastic Deformation of Crystalline Solids, Mellon Institute, Pittsburgh, (NAVEXOS-P-834), p. 150.
Fressengeas, C., Taupin, V., Capolungo, L., 2011. Int. J. Solids Struct. 48, 3499.
Fressengeas, C., Acharya, A., Beaudoin, A.J., 2011. In: Ghosh, S., Dimiduk, D. (Eds.), Computational Methods for Microstructure-Property Relationships. Springer, pp. 277–309.

Fressengeas, C., Taupin, V., Capolungo, L., Upadhyay, M., 2012. Int. J. Solids Struct. 49, 2660.
Fressengeas, C., Taupin, V., Capolungo, L., 2014. Int. J. Solids Struct. 51, 1434.
Gorkaya, T., Molodov, D.A., Gottstein, G., 2009. Acta Mater. 57, 5396.
Gutkin, M.Yu., Ovid'ko, I.A., 2005. Appl. Phys. Lett. 87, 251916.
Hasson, G., Boos, J.Y., Herbeuval, I., Biscondi, M., Goux, C., 1972. Surf. Sci. 31, 115.
Hecht, F., Pironneau, O., Le Hyaric, A., Ohtsuka, K., 2014. freefem++. <www.freefem.org/ff++/>.
Hirth, J.P., Pond, R.C., 1996. Acta Mater. 44, 4749.
Hirth, J.P., Pond, R.C., Lothe, J., 2006. Acta Mater. 54, 4237.
Khater, H.A., Serra, A., Pond, R.C., Hirth, J.P., 2012. Acta Mater. 60, 2007–2020.
Kleman, M., Friedel, J., 2008. Rev. Mod. Phys. 80, 61.
Kröner, E., 1980. In: Balian, R. et al. (Eds.), Phys. Defects. North Holland, Amsterdam, pp. 218–314.
Li, J.C.M., 1972. Surf. Sci. 31, 12.
Mach, J., Beaudoin, A.J., Acharya, A., 2010. J. Mech. Phys. Solids 58, 105.
McDowell, D.L., 2008. Mater. Sci. Eng. R 62, 67.
Mindlin, R.D., Tiersten, H.F., 1962. Arch. Ration. Mech. Anal. 11, 415.
Mompiou, F., Caillard, D., Legros, M., 2009. Acta Mater. 57, 2198.
Mura, T., 1963. Philos. Mag. 89, 843.
Nye, J.F., 1953. Acta Metall. 1, 153.
Ovid'ko, I.A., Sheinerman, A.G., Aifantis, E.C., 2008. Acta Mater. 56, 2718.
Pantleon, W., 2008. Scr. Mater. 58, 994.
Pond, R.C., Hirth, J.P., 1994. Solid State Phys. 47, 287.
Priester, L., 2013. Grain boundaries, from model to engineering. Springer Series in Material Science, vol. 172, 2013.
Puri, S., Das, A., Acharya, A., 2011. J. Mech. Phys. Solids 59, 2400.
Richeton, T., Wang, G.F., Fressengeas, C., 2011. J. Mech. Phys. Solids 59, 2023.
Romanov, A.E., Vladimirov, V.I., 1992. In: Nabarro, F.R.N. (Ed.), Dislocations in Solids, vol. 9. Elsevier, Amsterdam, p. 191.
Romanov, A.E., Kolesnikova, A.L., 2009. Prog. Mater. Sci. 54, 740.
Romanov, A.E., Kolesnikova, A.L., Orlova, T.S., Hussainova, I., Bougrov, V.E., Valiev, R.Z., 2015. Carbon 81, 223.
Rösner, H., Kübel, C., Ivanisenko, Y., Kurmanaeva, L., Divinski, S.V., Peterlechner, M., Wilde, G., 2011. Acta Mater. 59, 7380.
Shih, K.K., Li, J.C.M., 1975. Surf. Sci. 50, 109.
Sutton, A.P., Vitek, V., 1983. Philos. Trans. R. Soc. London A309, 1.
Taupin, V., Capolungo, L., Fressengeas, C., 2014. Int. J. Plasticity 53, 179.
Taupin, V., Berbenni, S., Fressengeas, C., 2012. Acta Mater. 60, 664.
Tschopp, M.A., Tucker, G.J., McDowell, D.L., 2007. Acta Mater. 55, 3959.
Tschopp, M.A., Spearot, D.E., McDowell, D.L., 2008. In: Hirth, J.P. (Ed.), Dislocations in Solids, vol. 14, p. 43.
Tucker, G.J., Tschopp, M.A., McDowell, D.L., 2010a. Acta Mater. 58, 6464.
Upadhyay, M., Capolungo, L., Taupin, V., Fressengeas, C., 2013. Philos. Mag. 93, 794.
Van Swygenhoven, H., Derlet, P.M., Froseth, A.G., 2006. Acta Mater. 54, 1975.
Van Swygenhoven, H., 2008. Mater. Sci. Eng. A 483–484, 33.
Vattre, A.J., Abdolrahim, N., Kolluri, K., Demkowicz, M.J., 2014. Nat. Sci. Rep. 4 (6231), 1–7.
Volterra, V., 1907. Ann. Sci. Ecol. Norm. Supp. III (24), 401–517.
Gertsman, V.Yu., Nazarov, A.A., Romanov, A.E., Valiev, R.Z., Vladimirov, V.I., 1989. Philos. Mag. A 59, 1113.